Journal of the European Ceramic Society 43 (2023) 4939–4949

Contents lists available at ScienceDirect

Journal of the European Ceramic Society

journal homepage: www.elsevier.com/locate/jeurceramsoc

Original article

Efficient modelling of ceramic sintering processes: Application to bilayers and membranes

Hao Shi [a,*], Diletta Giuntini [a,b], Hans van Dommelen [a], Marc G.D. Geers [a], Joris J.C. Remmers [a]

[a] Department of Mechanical Engineering, Eindhoven University of Technology, 5612 AZ, Eindhoven, The Netherlands
[b] Institute of Advanced Ceramics, Hamburg University of Technology, D-21073, Hamburg, Germany

ARTICLE INFO

Keywords:
Continuum modelling
Solid state sintering
Skorohod Olevsky Viscous Sintering (SOVS) model
Implicit integration
Bilayer ceramic
FEM
Lanthanum tungstate

ABSTRACT

The constitutive relation of Skorohod and Olevsky for viscous sintering is utilized to model the shrinkage and relative density evolution during the sintering process of ceramics. A new implicit integration scheme is presented and implemented. The computational cost is drastically reduced by combining this integration scheme with a solid-like shell element formulation, which also enables a faster and more accurate description of shape distortions, especially for thin geometries. The characterization and identification of the material viscosity is also improved via the Aquilanti–Mundim deformed Arrhenius description. The model robustness is examined with a spectrum of benchmark tests: ZnO sintering experiments from previous studies, as well as new lanthanum tungstate sintering tests. The model predictions for both dimensional shrinkage and relative density evolution are very accurate using the newly proposed material viscosity functions. The model improvements offer the possibility to simulate long-time sintering processes with higher accuracy and significantly reduced computational efforts.

1. Introduction

Ceramics are ubiquitous in our lives, from tableware to advanced and functional ceramics deployed in batteries, electronics, catalytic components, and thermal engines. A key step in the manufacturing of ceramics is solid-state sintering, upon which mass transfer mechanisms lead to reducing porosity in a compacted powder, resulting in the densification and shrinkage of the part [1]. Many issues can occur during this process: non-uniform densification and micro-cracking [2–4]; lack of control of the final microstructure and associated mechanical properties [5–7]; shrinkage anisotropy and inhomogeneous microstructures (particularly relevant with the advent of powder-based additive manufacturing (AM) processes [8–11]); distortions and cracking in composites [12–14]. The latter becomes particularly relevant in thin geometries, such as bi- and tri-layer membranes, which are receiving increasing attention for catalytic applications, where the variations of properties can be fine-tuned through their thickness [5,7,15]. Understanding and controlling each material's shrinkage behaviour and stress state during sintering is essential to tackle these problems. However, most sintering processes are designed based on costly and inefficient trial-and-error approaches. There is thus substantial interest in the development of robust, reliable and efficient predictive modelling frameworks for sintering processes [16].

Sintering can be modelled at different length scales with several methods: the Finite Element Method (FEM) at the continuum (macro)-scale [14,17–24], the Discrete Element Method (DEM) [25–31], the Phase-Field Method (PFM) [32–38] and the kinetic Monte Carlo (kMC) [39–42] at the meso/particle scale, or the combination of kMC/DEM and FEM in multiscale approaches [43]. DEM has the advantage of being mesh-free and of simulating the motion and morphology changes of each particle. However, this method typically assumes spherical particles and relies on a semi-empirical micro-mechanical model that needs micro-scale experiments for accurate parameter determination. It is also computationally demanding, due to the small time steps needed to resolve the contacts/collisions among particles, making the modelling of realistic, long-duration sintering processes almost unfeasible. The phase-field method relies on free energy minimization principles, and kinetic evolution equations. It is a good platform to model material flow and grain morphology evolution, capturing phenomena at the particle length scale, such as neck and grain growth. It is, nevertheless, equally or sometimes even more computationally demanding than DEM, since it requires adaptive meshing at inter-particle contacts to fully resolve the concentration gradients during material diffusion. The kinetic Monte Carlo simulations are computationally less expensive and also capture microstructural features, but their reliability

---

* Corresponding author.
E-mail addresses: h.shi1@tue.nl (H. Shi), d.giuntini@tue.nl (D. Giuntini), j.a.w.v.dommelen@tue.nl (H. van Dommelen), m.g.d.geers@tue.nl (M.G.D. Geers), j.j.c.remmers@tue.nl (J.J.C. Remmers).

https://doi.org/10.1016/j.jeurceramsoc.2023.03.053
Received 13 January 2023; Received in revised form 16 March 2023; Accepted 26 March 2023

strongly depends on the reconstruction of the initial 3D material microstructure, which is in most cases cumbersome to obtain. The finite element method is, instead, particularly advantageous: it has a lower computational cost and relies on well-established continuum theories of sintering. It enables reliable simulations of arbitrarily complex-shaped macro-scale components. This becomes particularly valuable for additively manufactured and composite parts, and for multilayered membranes, which typically do not shrink isotropically.

Most continuum-based theories are phenomenological, and they model the shrinkage of a green body during sintering via inelastic strains. A well-established theory is the Skorohod–Olevsky Viscous Sintering (SOVS) model [19]. It is based on the concepts of generalized viscous flow of porous bodies, and it is derived from a thermodynamical consistent continuum mechanics framework. A broad spectrum of applications, extensions, and refinements of the SOVS model is available in the literature [10,23,24,44,45], also proposing refined material viscosity functions [46], and incorporating micro-scale information via kMC parameters or grain growth functions [47]. Most of these works implement the SOVS equations into commercial FEM software, as nonlinear constitutive models and ODE subroutines [2,14,21,48,49]. The software is however not publicly accessible, and the numerical methods used to solve the governing equations are not always fully disclosed. Open access and flexible model implementations are thus called for. To the best of the authors' knowledge, there are only few attempts [47,50] to implement the SOVS theory in open and/or in-house developed FEM codes, and to subsequently evaluate the influence of solution algorithms on the models' accuracy and performance.

This work aims at developing a computationally efficient and versatile, (able to handle arbitrary geometries and materials) modelling platform that accurately predicts the evolution of powder compacts during sintering towards their final geometries. The article is thus structured as follows: Section 2 gives a brief introduction to the SOVS model, including a new method for the characterization of the viscosity of the powder material during sintering; the improved numerical integration scheme and its implementation are discussed in Section 3, followed by an introduction to solid-like shell elements (Section 4); results are discussed in Section 5, followed by conclusions and outlook (Section 6).

2. SOVS model formulation

The Skorohod–Olevsky viscous sintering (SOVS) model is a continuum mechanics-based modelling framework capturing the stress, strain and density evolution of a powder based material undergoing sintering, given that the constitutive behaviour of the powder material is specified. It is a phenomenological model whereby a porous medium is considered as a two-phase material that includes a porous body skeleton phase and a void phase. The skeleton is assumed to consist of individual particles having a general nonlinear viscous incompressible behaviour, and the voids are homogeneously distributed within the medium. As a consequence, the overall response is isotropic. We focus on the free (pressureless) sintering of μm-sized powders of functional oxides that are relevant for membrane and multilayered components (0.2 μm ZnO and 1.1 μm LaWO_{54}). For this case, a linear viscous description for the constitutive behaviour of the powder is appropriate, since the non-linear viscous behaviour only becomes dominant for pressure-assisted sintering and/or when the particle size is in the nm range [19,23,24].

Strain decomposition

The material behaviour is described by a standard decomposition of the total strain field $\boldsymbol{\varepsilon}$ into its elastic component $\boldsymbol{\varepsilon}_e$ and inelastic/viscous component $\boldsymbol{\varepsilon}_i$:

$$\boldsymbol{\varepsilon} = \boldsymbol{\varepsilon}_e + \boldsymbol{\varepsilon}_i \tag{1}$$

with its equivalent rate form:

$$\dot{\boldsymbol{\varepsilon}} = \dot{\boldsymbol{\varepsilon}}_e + \dot{\boldsymbol{\varepsilon}}_i \tag{2}$$

Linear elasticity

The stress state $\boldsymbol{\sigma}$ is connected to the elastic strain $\boldsymbol{\varepsilon}_e$ via Hooke's Law:

$$\boldsymbol{\sigma} = {}^4\boldsymbol{C} : \boldsymbol{\varepsilon}_e = \lambda \mathrm{tr}(\boldsymbol{\varepsilon}_e)\boldsymbol{I} + 2\mu\boldsymbol{\varepsilon}_e \tag{3}$$

with ${}^4\boldsymbol{C}$ - the fourth order stiffness tensor, and λ, μ - the Lamé coefficients.

Linear viscous formulation of the SOVS model

The original SOVS constitutive equation in its linear form reads [19]:

$$\boldsymbol{\sigma} = 2\eta\left[\phi\dot{\boldsymbol{\varepsilon}}_i' + \psi\dot{e}\boldsymbol{I}\right] + P_L\boldsymbol{I} \tag{4}$$

or in the inelastic (sintering) strain rate form:

$$\dot{\boldsymbol{\varepsilon}}_i = \frac{\boldsymbol{\sigma}'}{2\eta\phi} + \frac{\mathrm{tr}(\boldsymbol{\sigma}) - 3P_L}{18\eta\psi}\boldsymbol{I} \tag{5}$$

where $\boldsymbol{\sigma}$ is the Cauchy stress tensor, $\boldsymbol{\sigma}'$ the deviatoric stress tensor, $\dot{\boldsymbol{\varepsilon}}_i'$ the deviatoric inelastic strain rate tensor, $\dot{e} = \mathrm{tr}(\dot{\boldsymbol{\varepsilon}}_i)$ trace of inelastic strain rate tensor or volume shrinkage rate, η the viscosity of the fully dense skeleton (powder) phase, ϕ the normalized shear viscosity, ψ the normalized bulk viscosity, P_L the (effective) volume sintering stress[1] [24,51].

The main terms of Eqs. (4) and (5) depend on temperature and relative density as follows [39,42,52]:

$$\phi(\rho) = \rho^2 \tag{6}$$

$$\psi(\rho) = \frac{2}{3}\frac{\rho^3}{1-\rho} \tag{7}$$

$$P_L(\rho) = \frac{3\alpha}{r_p}\rho^2 \tag{8}$$

where ρ is the relative density (equivalent to solid volume fraction), the ratio between bulk and skeleton densities $\rho_b/\rho_{skeleton}$, reaches 1 for the fully sintered body; ρ_b is the bulk density, the ratio between the solid mass and the total volume of geometry including the internal voids M_s/V_t. The normalized bulk and shear viscosities are functions of the porosity and are derived using the hydrodynamic analogy to the theory of elasticity. The sintering stress P_L is defined as directly proportional to the material's surface tension, α, and inversely proportional to the powder particle radius, r_p, and it is thus a local function or surface tension acting at the single pore's interface, while it also has a relative density dependency to account for the macroscopic averaged effects of all the pores in the considered domain [19,24].

Evolution of the relative density

The volume shrinkage rate is connected to the relative density employing the following continuity equation:

$$\dot{\rho} = -\rho\dot{e} \tag{9}$$

Material viscosity dependency on temperature — quadratic function

Olevsky et al. [42] proposed to describe the material viscosity dependency on temperature with a quadratic equation as given in

---

[1] Note that the sintering stress is defined as the hydrostatic (compressive) stress which can stop the shrinkage when it is imposed in the opposite direction, and thus represents the internal driving force magnitude ($P_L \geq 0$).

Eq. (10).

$$\eta(T) = a(\frac{T}{T_0})^2 + b\frac{T}{T_0} + c \tag{10}$$

with T_0 - the initial/starting ambient temperature of the sintering process; a, b and c are coefficients of the temperature function. To determine the coefficients of a specific material, i.e. ZnO powder, the procedure involves multiple cyclic loading sintering experiments.

Material viscosity dependency on temperature - Arrhenius functions

Although the material viscosity function expressed as in Eq. (10) can capture well the viscosity evolution in certain temperature ranges during sintering, it is in general not fully representative of the physics underlying the sintering process, i.e. its thermal activation. This polynomial approximation is empirically based on the measured viscosity during solid state sintering of ZnO powder, but it is not immediately generalizable to the more complex material behaviour occurring during sintering, e.g., liquid phase formation, phase transformations, etc. The adopted Arrhenius-type description is, instead, capturing the thermal activation aspects, and it is of more general applicability, also in terms of sintering temperature ranges.

Reiterer et al. [46] proposed to describe the material viscosity's dependency on temperature through a classical Arrhenius-type function, and it has been used for modelling the bilayer sintering of cerium gadolinium oxide (CGO) powder [21]. Torresani et al. [11] recently proposed a simpler method for determining the material viscosity, using the shrinkage data from mechanical dilatometry combined with a quadratic Arrhenius function. Here, we propose to use the Aquilanti–Mundim deformed Arrhenius function [52], which is flexible and versatile in describing the temperature dependency over a wide range.

Assuming the material's shrinkage is isotropic during free sintering, the trace of inelastic strain rate tensor $\dot{e}$ can be directly calculated from the displacement field and time span measured via dilatometry. The material viscosity can then be estimated by combining Eqs. (5), (7) and (8):

$$\eta = \frac{1}{4}\frac{1-\rho}{\rho}\frac{\alpha}{r_p \dot{e}} \tag{11}$$

Once the material viscosity is calculated from the dilatometry shrinkage data using Eq. (11), the temperature data from the same experiment can also be exploited to reveal the relationship of $\eta(T)$, which is still in the form of discrete data points. For the sake of convenience, we use the reciprocal of the normalized temperature T^*, which is defined as $1/T^* = 1/T - 1/T_T$, with T_T defined as transition/characteristic temperature at which the sintering starts and the material viscosity drops drastically. Then, the deformed Arrhenius function is finally used to describe the material viscosity dependency on temperature [52] using these discrete experimental data points (replacing the relationship shown in Eq. (10)):

$$\eta(T^*) = \eta_0 \exp_d\left(\frac{-\gamma}{RT^*}\right) = \eta_0\left[1 - d\frac{\gamma}{RT^*}\right]^{\frac{1}{d}} \tag{12}$$

Here, the coefficient R is the universal gas constant, η_0 and γ (same units as RT^*) are material-dependent constants, and d is the deformed parameter. Note that in the limit of $d \to 0$, $\gamma \to E_a$ (activation energy), the standard Arrhenius function is recovered.

3. Numerical integration scheme and implementation

In current study, an in-house FEM code/software, namely "DAWN" is used. This is a C++ finite element code that comprises a variety of element formulations, materials and solver techniques, most of which are not available in commercial or open-source codes. The methods proposed here are nevertheless general and can be applied to any FEM software, both commercial and open source.

As with any 3D constitutive model intended for use with finite element codes, an accurate, robust, and efficient numerical routine is needed. For the current SOVS sintering model, Eq. (5) reveals that the direction and magnitude of inelastic strain depend directly on the stress state. Thus, conventional routines as used in visco-plasticity models cannot be directly utilized. Here, we implement the SOVS model using a fully implicit Euler time integration scheme with variable reductions to explore predictability and computational efficiency.

Implicit scheme for time integration

From Eqs. (2), (5), (9) we have three unknown state variables, $\boldsymbol{\varepsilon}_e$, $\boldsymbol{\varepsilon}_i$ and ρ, which needed to be solved for in both space and time.[2] The evolution of these state variables is governed by a system of ODEs. It can be expressed in a general form:

$$\dot{\underset{\sim}{X}} = \mathcal{F}(\underset{\sim}{X}, \underset{\sim}{\xi}) \tag{13}$$

where $\underset{\sim}{X}$ is the column of unknown variables, decomposed as following:

$$\underset{\sim}{X} = \begin{bmatrix} \boldsymbol{\varepsilon}_e \\ \boldsymbol{\varepsilon}_i \\ \rho \end{bmatrix} \tag{14}$$

$\underset{\sim}{\xi}$ in Eq. (13) is a placeholder for the external state variables that vary independently of the SOVS model, e.g., the temperature T. $\boldsymbol{\varepsilon}_e$ and $\boldsymbol{\varepsilon}_i$ are elastic and inelastic strain tensors, but for the implementation we use Voigt notation and result in two sub-columns with length 6.

Backward Euler integration scheme

In one timestep, $\Delta t = t^{n+1} - t^n$:

$$\underset{\sim}{X}^{n+1} = \underset{\sim}{X}^n + \Delta t\mathcal{F}(\underset{\sim}{X}^{n+1}, \underset{\sim}{\xi}^{n+1}) \tag{15}$$

Then the corresponding residual is:

$$\mathcal{R}(\Delta\underset{\sim}{X}) = \Delta\underset{\sim}{X} - \Delta t\mathcal{F}(\underset{\sim}{X} + \Delta\underset{\sim}{X}, \underset{\sim}{\xi} + \Delta\underset{\sim}{\xi}) \tag{16}$$

with

$$\Delta\underset{\sim}{X} = \begin{bmatrix} \Delta\boldsymbol{\varepsilon}_e \\ \Delta\boldsymbol{\varepsilon}_i \\ \Delta\rho \end{bmatrix}$$

and

$$\mathcal{F}(\Delta\underset{\sim}{X}) = \begin{bmatrix} \boldsymbol{f}_{\varepsilon_e} \\ \boldsymbol{f}_{\varepsilon_i} \\ f_\rho \end{bmatrix}$$

This set of residual equations, Eq. (16), is solved using the Newton–Raphson procedure. To apply the Newton–Raphson procedure on this set of equations, the 13 unknowns in $\underset{\sim}{X}$ have to be solved in an iterative manner, which requires a computationally costly inversion of a 13 × 13 Jacobian matrix in each iterative solve step (the Newton–Raphson iteration steps within one single timestep). In addition, this iterative solution routine has to be performed on each material/integration point within every element of the mesh to obtain a correct stress response. Accordingly, the computational cost grows rapidly when one has to deploy a finer mesh to resolve the geometry in more detail. Therefore, we propose to first eliminate the relative density (1 unknown $\Delta\rho$) from the solution routine via explicit calculations. Next, the inelastic strain is reduced from 6 unknowns to 1 unknown by assuming isotropic shrinkage behaviour. This assumption is also valid for complex geometry or loading conditions made of the same isotropic material. Finally, the remaining 7 unknowns (6 components from the elastic strain $\Delta\boldsymbol{\varepsilon}_e$ and

---

[2] The elastic and inelastic strain are tensors, each has 6 independent scalar values, thus 13 scalar unknown values in total.

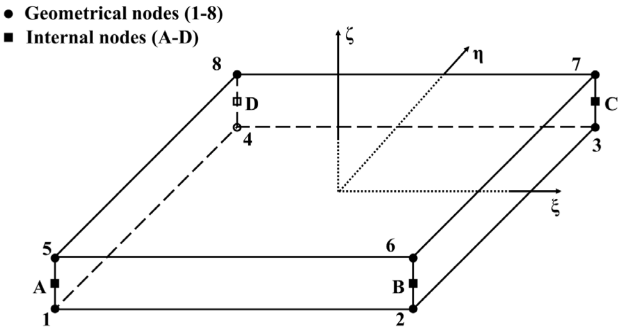

Fig. 1. Geometry of the eight nodes solid-like shell element [56,57]. Each geometrical node i contains three degrees of freedom: $[u_x, u_y, u_z]^i$ and each internal node j has one degree of freedom w^j.

1 inelastic strain Δe) is further reduced to a single unknown Δe, using the linearity between stress $\boldsymbol{\sigma}'$ and strain deviators $\boldsymbol{\varepsilon}_i'$. The derivations are explained in detail in Appendix. After the determination of the change of inelastic strain, the change of elastic strain can be calculated from the change of total strain, and the material's stress state can be determined.

4. Solid-like shell element

Advanced ceramic manufacturing processes nowadays incorporate complex structures and geometries, such as composite materials, multilayered materials, 3D-printed complex shapes, thin layered catalytic ceramic membranes, etc., requiring a suitable element for the finite element modelling of their sintering behaviour. Conventional linear solid (Small Strain Continuum — SSC) elements, e.g., eight nodes hexahedral element, show an overly stiff behaviour when used in thin domains applications (Poisson thickness locking [53]) due to a constant strain distribution in the thickness direction. An alternative is the Solid-Like Shell (SLS) element [54,55], for which an additional set of internal degrees of freedom is used to add a quadratic term to the displacement field in the thickness direction, the internal 'stretch' of the element, as shown in Fig. 1. Three translational degrees of freedom are defined at each node as for typical solid elements, and four internal degrees of freedom are established at the through-thickness edges of the element to account for the internal stretching, which yields a fully three-dimensional bending strain field.

The corresponding strain field varies linearly over the thickness instead of being constant, and Poisson thickness locking is avoided. Additionally, the SLS element is a true 3D solid element that allows for a 3D constitutive relation, which is typically not possible for the other 2D or pseudo-3D shell element formulations. It has been shown that the solid-like shell element can be used for modelling laminate structures by either stacking multiple elements or by modelling multiple layers within one element [56–58]. In the latter situation, the element is divided into several sub-domains, each of which has different material parameters. Both conventional volume elements and solid-like shell elements are here used with the SOVS material model, to explore the feasibility, performance and efficiency of the sintering modelling framework.

5. Results and discussion

The SOVS sintering model described in the previous Sections Section 2 & 3 with both original and reduced integration schemes is implemented into our in-house FEM software "DAWN". In Section 5.1, the accuracy of the model implementation is verified with a test case on two elements, by comparing the numerical results with a closed-form analytical solution as well as a semi-analytical solution obtained via alternative numerical integration methods. In Section 5.2, the performance and accuracy of the numerical model is assessed by comparing the numerical results obtained with the two element types with experimental data on a bilayer bar. In Section 5.3, the model's accuracy in predicting the differential shrinkage-induced bending behaviour of layered materials is validated by comparing the numerical outcomes with experimental data from the literature on the sintering of bilayer discs, with quadratic viscosity function given by Eq. (10). Finally, in Section 5.4, the broad applicability of the model is assessed by extending it to another functional ceramic material (lanthanum tungstate) with the Aquilanti–Mundim deformed Arrhenius viscosity function given by Eq. (12) in Section 2. The model predictions are quantitatively verified with a simple sintering experiment that covers the entire heating, holding and cooling stages.

5.1. *Verification of model implementation with analytical solutions*

Inspired by the SOVS model verification published in [47], a simple test case with two identical solid elements (8-nodes Hexahedron) is used for the first verification step, as given in Fig. 2. The material here is a powder compact of 0.2 μm ZnO particles, in line with Olevsky et al. [39,42] and Argüello et al. [47]. The material and sintering bilayer disc parameters are $E = 123.7$ GPa, $\nu = 0.356$, $\alpha = 1.27$ J/m^2, $r_p = 0.2$ μm. The starting and ending temperatures of the sintering process are $T_0 = 750$ °C and $T_{end} = 1000$ °C. The heating ramp is 5 °C/min. For this case study, the viscosity is expressed according to the quadratic form proposed by Olevsky et al. as given in Eq. (10), with $a = 51.7\times10^{10}$ Pa·s, $b = -106.6\times10^{10}$ Pa·s, and $c = 56.4\times10^{10}$ Pa·s [42]. The initial relative density is $\rho_0 = 47\%$. The left bottom node is fully constrained and the two elements are subjected to symmetry boundary conditions along their x-z and y-z planes. Two loading cases are studied here: free sintering with no externally applied stress and sintering with 5 MPa tensile stress applied on the top surface (z-direction).

For the free sintering case, the externally applied stress field is zero, thus Eq. (4) is simply expanded and results in the following governing equation of relative density evolution:

$$\dot{\rho} = \frac{3P_{L0}(1-\rho)}{4\eta(T)} \tag{17}$$

with $P_{L0} = 3\alpha\rho_0^2/r_p$ and $\eta(T)$ given by Eq. (10).

The closed form solution of Eq. (17), i.e. relative density evolution, is then given as reported in [47],

$$\begin{aligned}
\rho(t) &= 1 - \frac{(1-\rho_0)}{F}\exp\left\{-\frac{3}{4}P_{L0}\left[\frac{2}{\sqrt{Q_0}}\tan^{-1}\left(\frac{2C_0t+B_0}{\sqrt{Q_0}}\right)\right]\right\}\\
F &= \exp\left\{-\frac{3}{4}P_{L0}\left[\frac{2}{\sqrt{Q_0}}\tan^{-1}\left(\frac{B_0}{\sqrt{Q_0}}\right)\right]\right\}\\
Q_0 &= 4A_0C_0 - B_0^2\\
A_0 &= a+b+c\\
B_0 &= a\frac{10}{60T_0} + b\frac{5}{60T_0}\\
C_0 &= a\frac{25}{3600T_0^2}
\end{aligned} \tag{18}$$

with the values of a, b, c and T_0 as specified above.

For the sintering case with applied stress, a tensile stress is applied along the z-direction ($\sigma_{zz} = 5$ MPa, $\sigma_{xx} = \sigma_{yy} = 0$), and the continuity equation of the relative density evolution is given by

$$\dot{\rho} = \frac{\sigma_{zz}}{4\eta(T)}\frac{1-\rho}{\rho^2} - \frac{3P_{L0}(1-\rho)}{4\eta(T)} \tag{19}$$

The solution for Eq. (19) is found with an explicit Runge–Kutta (RK45) method, with error control of the fourth-order method, and steps using the fifth-order accurate formula (local extrapolation is done). The time step Δt is chosen as 6 s, which is sufficiently small to give accurate integration results. The relative density evolution of the ZnO powder

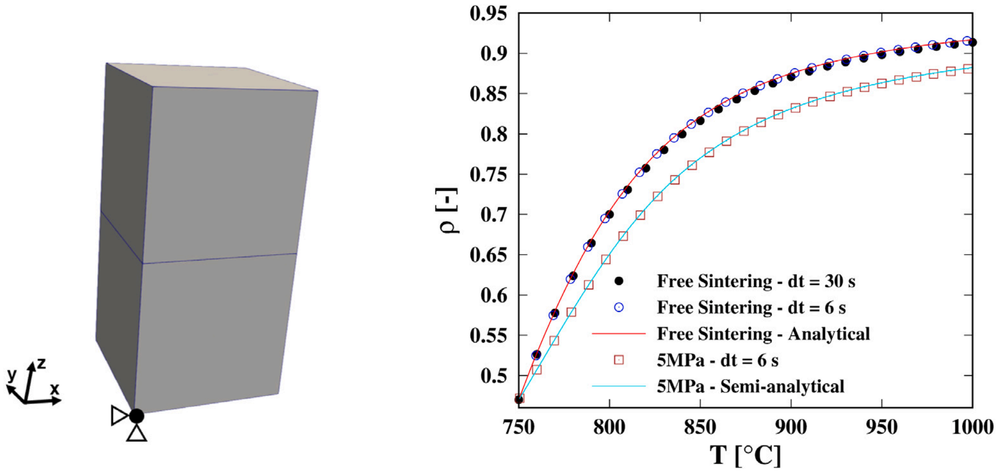

Fig. 2. Model verification by comparison of a two-element domain sintering shrinkage prediction with the analytical solution. Left: Geometry of the two-element domain. Right: Relative density evolution during sintering of ZnO with different loading conditions (free sintering and sintering with 5 MPa tensile stress). Lines are analytical solutions and points are simulation outputs. A time step $\Delta t = 30$ s corresponds to a temperature step $\Delta T = 2.5$ °C (with heating rate 5 °C/min).

compact during sintering is shown in Fig. 2. An excellent agreement between analytical, semi-analytical and the numerical solution is found, confirming the accuracy of the simplified implicit integration scheme. If the time step is reduced from $\Delta t = 30$ s to 6 s, the difference between simulation and analytical solution is negligible. Unless otherwise specified, the time step $\Delta t = 30$ s will be used for the following analyses, as the error is small and the computational cost reduces by a factor of 5. For the case of sintering with an applied tensile stress, as expected, the shrinkage is slower than in the free sintering case, due to the tensile stress acting in the opposite direction of the (effective) volume sintering stress.

5.2. Benchmark test: model performance using solid and shell elements

The previous section proves the fidelity of the model implementation at the element (integration points) level. To test the model validity in real-scale sintering processes and the performance of the implementation with shell elements, a larger scale and more complex study domain is used. A relevant test case that was also studied in previous works [42,47,59], is the sintering of a bilayer bar [59]. The same material as in Section 5.1 is considered (ZnO), but this time in two layers with different initial relative densities, which leads to differential shrinkage rates. The bilayer bar consists of two rectangular blocks with initial length $L = 8.049$ mm; width $W = 3.89$ mm and equal thickness of upper and lower layer $H_u = H_l = 1.316$ mm (taken from [59]), as given in Fig. 3. The upper and lower layer have initial relative densities of 47% and 57%, respectively. The sintering process parameters (heating rate, temperature range, etc.) are identical to those in the case of the two-element model of Section 5.1. Note that the geometry in Fig. 3 only represents a quarter of the original geometry and symmetry boundary conditions are applied at the x-z and y-z planes.

To compare the computational cost for the different element types (solid element versus solid-like shell element), the bilayer bar test-case shown here is simulated using both element types. The SLS element has 8 nodes on the element boundaries and 4 additional internal nodes along the thickness direction to model the stretching (Fig. 1), and it is thus much more suitable to simulate bending problems, as required here.

Table 1
Sintering of ZnO bilayer bar: Garino's experimental data [59] vs. simulation outcomes obtained using solid-like shell (SLS) elements.

Dimensions [mm]	Exp. @ 1000 °C	Sim. @ 1000 °C	Error [%]
L	6.70	6.67	0.4
W	3.89	3.73	3.3
H	2.15	2.06	3.6

The results of numerical simulations with SLS and SSC elements are compared with experimental data from the literature [42,59], as shown in Fig. 3. Both simulations using SLS elements (bottom left) and SSC elements (bottom right) have same meshes with 928 8-node hexahedrons. The final bilayer bar curvature obtained with SLS elements agrees well with the experimental outcome: the upper layer has a lower initial relative density, which leads to faster shrinkage compared to the bottom layer, resulting in the final upward bending. The results obtained with SSC elements, instead, show almost no bending, due to the locking of the linear elements, even with a relatively fine mesh. The simulated final relative density is also different in the two cases. A clear relative density gradient is observed in the SLS case, along the thickness (z) direction, with increasing relative density towards the concave (upper) surface. This gradient is not observed in the SSC case, and the final relative densities remain uniformly distributed in each layer. Even though the reference literature study does not report the final relative densities of each layer, the experimentally measured dimensions after sintering can be used for further validation [47,50,59]. The results are summarized in Table 1. A very good agreement between experiments and simulations is obtained, with an error range between 0.4 and 3.4%, which is comparable with the error range (0.1 to 4.0%) obtained in previous studies [47,59].

To obtain such accurate results, however, a fine mesh with 46080 solid elements was previously needed for the same bilayer bar simulation, with a resulting computational cost (CPU time) in the order of 10^5 seconds [47]. This is more than a day of simulation time, thus much longer than the 50-min sintering process time. In this work, the simulations are performed with 928 SLS elements and the improved time integration scheme. The computational cost is reduced by 3 orders of magnitude, resulting in a CPU time of 43.49 s, without sacrificing accuracy. Moreover, the memory needed for the sintering simulations is also drastically reduced, since the number of elements is decreased by a factor of approx. 50. This opens the pathway towards simulating long holding-time sintering processes without the demand of large computational infrastructures.

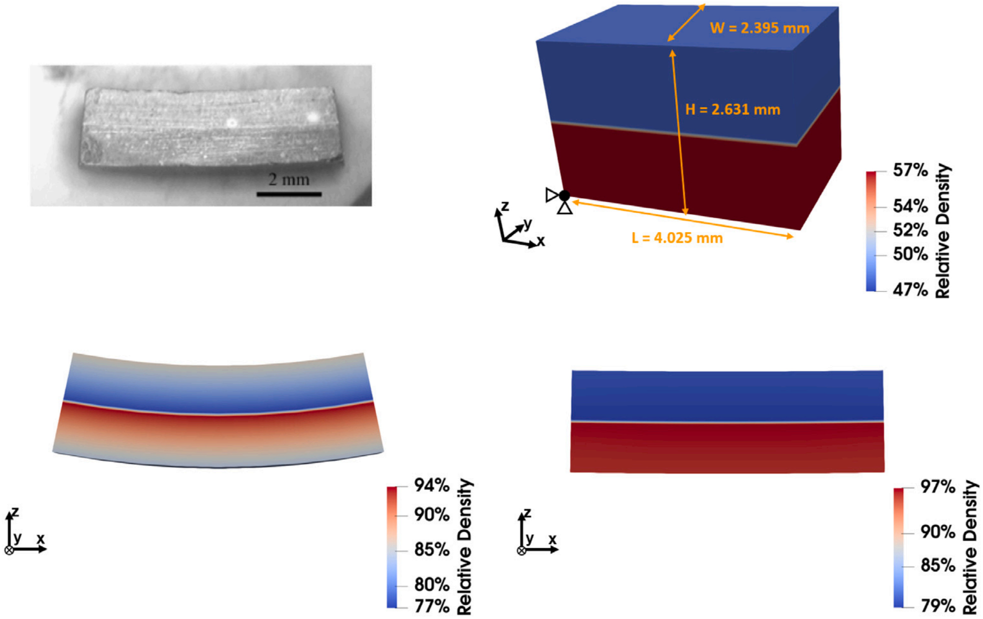

Fig. 3. Sintering of a ZnO bilayer. Top left: sintering experiment of bilayer bar ZnO at 1000 °C [42]. Top right: initial geometry and relative density of the bilayer bar: $\rho_u = 47\%$ and $\rho_l = 57\%$. Bottom: deformed configurations using Solid-Like Shell/SLS (left) and solid/SSC (right) elements.
Source: Reproduced with permission from John Wiley and Sons.

5.3. Prediction of differential shrinkage: Sintering of bilayered ZnO discs

The bilayer bar investigated in the previous section has an aspect ratio (length/thickness) of around 3 and the differential shrinkage-induced bending behaviour is not fully representative of many applications. In line with [47], to better evaluate the bending behaviour of such bilayered components, thin geometries with higher aspect ratios are more appropriate, such as the ZnO bilayer disc sintering experiment by Garino [47,59]. Fig. 4 shows this case study, with a bilayered disc with an aspect ratio of around 9. The disc consists of two layers with an initial radius R = 9.525 mm and equal thickness of the upper and lower layer, $H_u = H_l$ = 1 mm. The upper and lower layers have initial relative densities of 47% and 57%, respectively. The sintering process parameters (heating rate, temperature range, etc.) are identical to those of the bilayer bar case in the previous subsection. Similarly, symmetry boundary conditions are applied, using 1536 SLS elements to reduce the computational cost. The simulation results relative to 925 °C are shown in Fig. 4, revealing the displacement in the z direction (dZ) and the relative density. The displacement dZ increases along the radial direction, with a minimum of −0.38 mm at the centre of the disc, and reaching a maximum of 1 mm at the bottom edge. As expected, a more prominent bending is observed here compared to the bilayer bar case. As for the relative density field, a similar increasing gradient along the z direction is also observed, with density values lower in each layer compared to the bilayer bar. However, a relative density gradient is now also observed along the radial direction. The relative density increases slightly from the centre to the edge of the quarter disc. This small gradient along the radial direction is expected to be caused by the stress state: higher tensile stress at the bottom centre surface due to upward bending, thus hindering the shrinkage and leading to a lower final relative density. This agrees well with the lower final relative density obtained from the previous element test under 5 MPa tensile load. To quantify the overall sintering shrinkage, we monitor four characteristic geometrical parameters, defined in the bottom right of Fig. 4: centre thickness H_C (bending), bottom radius R_B (radial shrinkage of lower layer), top radius R_T (radial shrinkage of the upper layer) and edge thickness H_E (shrinkage in the thickness direction).

These dimensions are extracted from the simulation outcomes at 925 °C and compared with the experimental values, as summarized in Table 2. The bilayer disc simulations capture the shrinkage very accurately in both radial and thickness directions, with an error ranging from 0.9 to 3%. The prediction of disc bending is less accurate (7.6% error) but still much smaller than the 13.7% error obtained in previous studies that using solid elements [47,59]. The final dimensions of radii (R_T and R_B) and edge thickness H_E are somewhat smaller than those obtained experimentally in Garino's experiments, indicating a small over-prediction of the overall shrinkage. Although the error for the centre thickness (H_C) is smaller than in previous studies, the overall bending behaviour is still underestimated. A potential reason for this underestimation is the viscosity function for ZnO (and in [47,50]), which is taken from [42] directly, and which might underestimate the experimental viscosity of ZnO. Another possible cause could be the inaccurate initial relative density of each layer before sintering, which could easily lead to the mismatches observed here.

Table 2
Sintering of ZnO bilayer disc: Garino's experimental data [59] vs. simulation outcomes obtained using solid-like shell (SLS) elements.

Dimensions [mm]	Exp. @ 925 °C	Sim. @ 925 °C	Error [%]
R_T	7.62	7.33	3.0
R_B	7.83	7.75	0.9
H_E	1.63	1.59	2.1
H_C	2.72	2.57	7.6

5.4. Predicting the shrinkage of LWO powder compacts with a new viscosity characterization method

For a thorough verification of the new viscosity characterization approach proposed in Section 2 and its versatility, we have conducted a new set of sintering experiments, focused on accurate measurements of both shrinkage and relative density changes during the process. The material is another functional oxide powder: lanthanum tungstate ($LaWO_{54}$), which is currently particularly relevant for catalytic membranes.

Lanthanum tungstate powder ($LaWO_{54}$) is first uni-axially compressed (40 kPa) into cylindrical pellets and then hydro-statically compressed (400 MPa) to induce isotropic compaction. The resulting pellet

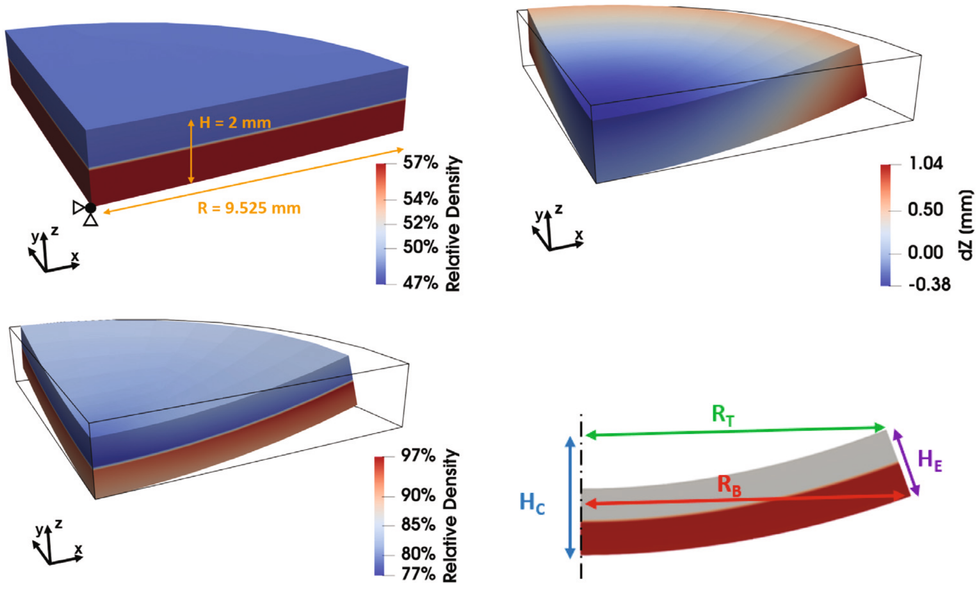

Fig. 4. Modelled shrinkage and bending of bilayered ZnO disc during sintering. Top left: initial (quarter) geometry bilayer of the simulation domain, with relative densities in the two layers $\rho_u = 47\%$ and $\rho_l = 57\%$. Top right: Displacement field in the z-direction at 925 °C. Bottom left: Relative density distribution at 925 °C. Bottom right: Final geometry after bending, with centre thickness H_C, bottom radius R_B, top Radius R_T and edge thickness H_E [59].

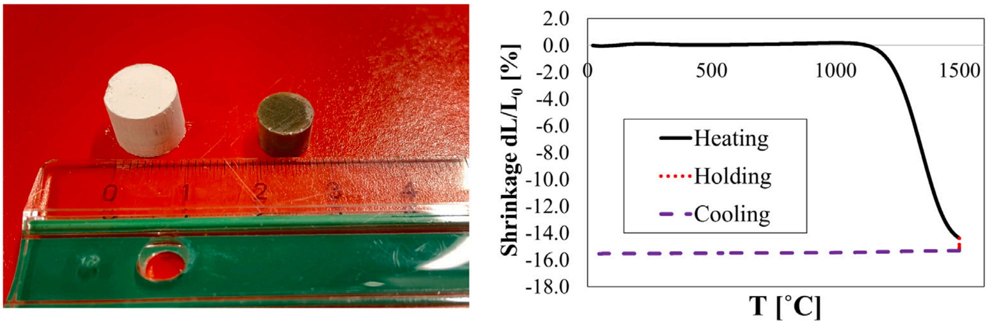

Fig. 5. Left: $LaWO_{54}$ pellet before and after sintering. Right: Densification/shrinkage of $LaWO_{54}$ pellet vs. sintering temperature, as measured by dilatometry.

has an initial relative density of 59.7%, as shown in Fig. 5. The $LaWO_{54}$ powder has median particle size $r_p = 1$ μm, theoretical density $\rho_s = 6.64$ g/cm^3, surface tension $\alpha = 1$ J/m^2, Young's modulus $E = 130$ GPa and Poisson's ratio $\nu = 0.24$. The sintering process is conducted with a mechanical dilatometer (Netzsch - DIL402C) and consists of the following stages: (i) heating stage, $T_0 = 25$ °C to $T = 1500$ °C at 2 °C/min; (ii) holding stage, $T = 1500$ °C for 720 mins; (iii) cooling stage, $T_{end} = T_0 = 25$ °C at −2 °C/min. The final sintered part is also shown in Fig. 5. The long holding stage allows to reach the final stage of sintering, i.e. approaching full density. This experimental setting offers the possibility to validate the model predictions not only in terms of dimensional changes (as most previous studies did) but also in terms of the evolution of relative density throughout the whole sintering process. The shrinkage, dL/L_0, with respect to sintering temperature that is given in Fig. 5.

The viscosity evolution of $LaWO_{54}$ and the corresponding viscosity functions, based on Eq. (12), are given in Fig. 6. To construct the Arrhenius model, we use the normalized temperature $1/T^* = 1/T - 1/T_T$ (defined in Section 2), with T_T defined as the transition temperature at which the sintering starts and the material viscosity drops drastically. For the $LaWO_{54}$ used here, T_T is 1005 °C, resulting in $1/T^* < 0$ when the sintering temperature is higher than the transition temperature, i.e. when $T > 1005$ °C.

For temperatures below T_T ($1/T^* > 0$), the viscosity of $LaWO_{54}$ stays almost constant around 3×10^{13} Pa·s, but increases to around

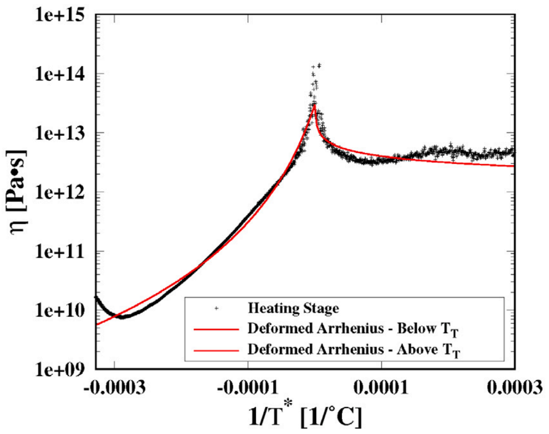

Fig. 6. Viscosity (η) of $LaWO_{54}$ as a function of temperature, plotted with respect to the reciprocal of normalized temperature ($1/T^*$), as determined from dilatometry. The lines correspond to the deformed Arrhenius functions, Eq. (12), with $\eta_0 = 2.975 \times 10^{13}$ Pa·s; $d = -2.791$, $\gamma = 7965$ kJ/mol for temperature below T_T and $d = -0.226$, $\gamma = 665$ kJ/mol for temperature above T_T. $T_T = 1005$ °C is determined from the maximum value of viscosity during sintering.

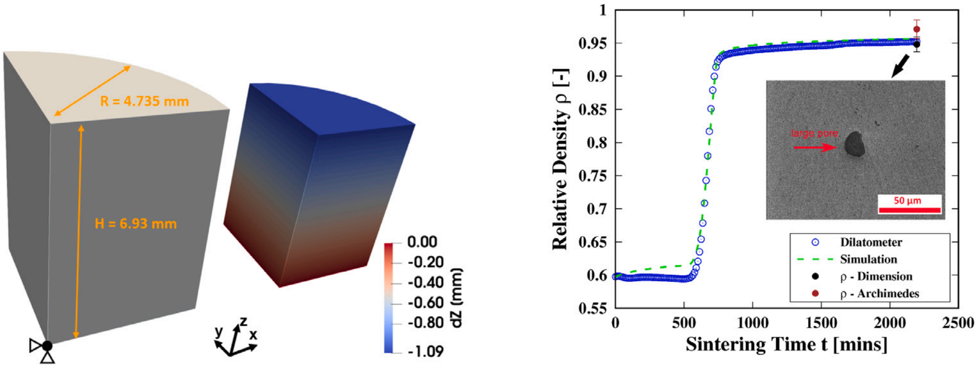

Fig. 7. Left: Initial and final simulated geometry of the pellet, before and after the 2196-min sintering process. The colour bar indicates the displacement [mm] in the thickness (z) direction. 3888 solid elements are used, with symmetry boundary conditions along the x-z and y-z planes. Right: Relative density evolution during sintering of $LaWO_{54}$ pellet - experiments vs. simulation. Inset: SEM image of the final sintered $LaWO_{54}$ pellet microstructure.

1×10^{14} Pa·s when $1/T^*$ is getting close to zero. For temperatures above T_T ($1/T^* > 0$), the viscosity decreases from a maximum value to around 1×10^{10} Pa·s with increasing sintering temperature T. The deformed Arrhenius function $\eta(T)$ adequately captures the viscosity dependency on temperature. The initial increase followed by a decrease of the viscosity could be caused by different material phases at different temperatures. As studied in [60], at temperature below T_T, the powder pellet may have the La_2O_3 phase embedded with $LaWO_{54}$ phase, and this La_2O_3 phase transforms into $LaWO_{54}$ phase with increasing temperature, in line with the initial increase of the viscosity. While for temperatures above T_T, the solid state sintering process is activated and the material starts to flow, i.e. a decrease in viscosity is observed. Note that in the low temperature branch ($1/T^* > 0$), the activation energy γ strongly depends on the amount of data included in this range since at lower temperatures sintering has not started yet. Here, the upper limit is set as $1/T^* \leq 0.0003$. The low-temperature branch is included in Fig. 7 for completeness, but at $T < 800$ °C ($1/T^* > 0.0003$ or $t > 400$ mins) almost no sintering shrinkage happens.

In addition to the heating stage, holding and cooling stages are also involved in the viscosity analysis. During the holding stage, the temperature is held constant at 1500 °C, and thus Eq. (12) cannot capture the viscosity changes that are associated with microstructural (and potentially phase) changes under isothermal conditions, as it only gives a single viscosity value at a given temperature. The viscosity increases as the sintering proceeds during the isothermal holding, while pores keep shrinking. In the final stage of sintering, grain growth occurs, and viscosity can strongly depend on grain size and other microstructural features. To accurately determine the grain growth and additional microstructural changes during material sintering, thorough experimental campaigns would be required. Therefore, we instead propose to add this additional dependency on the microstructure evolution indirectly, by adding a dependency of viscosity on the relative density during holding: $\eta(\rho) = \eta(T^*) \cdot 10^{(\rho-\rho_0)/\Delta\rho*\beta}$ with $\rho_0 = 92\%$, $\Delta\rho = 0.02$, $\beta = 1.33$, whereby the coefficients are obtained from dilatometry data. During the cooling stage, the viscosity increases again with decreasing temperature, and thus the deformed Arrhenius function can be applied again.

Given this viscosity formulation, $LaWO_{54}$ properties and sintering process parameters, the simulation is implemented with a quarter pellet and the appropriate symmetry conditions, as shown in Fig. 7. The geometry after sintering is also given, with the displacement field in the z-direction (dZ), in the same figure. The displacement dZ decreases smoothly with the height and reaches a minimum of −1.1 mm (maximum shrinkage) at the top of the pellet. The other two displacement fields, dX and dZ, show a similar trend. Since in this case, the pellet is homogeneous, no differential shrinkage is expected, and thus 8-node SSC elements are used instead of SLS elements. This further reduces the computational cost, thanks to the lower number of integration points per element. The final pellet dimensions after sintering for both experiments and simulations are summarized in Table 3. The model slightly overestimates the shrinkage in the radial direction (1.5% error) and underestimates the shrinkage in the thickness direction instead (2.9% error). These small discrepancies can arise from the small stress applied by the dilatometer's push-rod in the experiments. Even though free sintering is conducted, in the dilatometer the push-rod needs to be in contact with the surface of the pellet throughout the whole sintering process, and thus a small force (25 cN) is applied along the thickness direction.

Table 3
Sintering of $LaWO_{54}$ pellet: experiment vs. simulation.

Dimensions [mm]	Exp.	Sim.	Error [%]
R	8.10	7.98	1.5
H	5.68	5.84	3.0

The relative density changes in experiments and simulations are also compared in Fig. 7. According to dilatometry data (blue circles), the relative density, ρ, increases from 59.7% to 95.2% after the cooling stage, at $t = 2196$ mins. The simulation (dashed line) adequately captures the evolution of the relative density throughout the whole sintering process, giving a final relative density prediction of 95.7%, and thus resulting in a 0.4% error compared to the experiments. Even with a relatively long holding time (12 h), the shrinkage process appears to stop before the pellet reaches its full density. To investigate the dominating mechanism behind this, the final sintered pellet is polished and scanned using SEM with a 1 kV accelerating voltage. The inset of Fig. 7, a representative micrograph, reveals a large-sized pore, surrounded by fully densified $LaWO_{54}$. Such large-sized, spherical pores are well-known to be a cause of incomplete densification due to extremely slow shrinkage kinetics [61,62]. Furthermore, the final density of the sintered pellets has been measured via two different methods: geometry-based, i.e. as weight/volume ratio (black filled circle) and via the Archimedes method (brown filled circle). Although the final relative density from the Archimedes method is slightly higher than that from the geometry-based method, the outcomes of both methods are consistent with the model predictions, further proving the validity of the proposed modelling method. Note that measuring the initial/final relative density accurately is not always as easy as in the case presented here, since many sintering applications involve binders, additives other than ceramics or require a porous final microstructure, such as for catalytic membranes and substrates, fuel cells, battery electrodes, etc. [5]. In these cases, the characterization of initial/final relative densities, both with and without differential shrinkage, becomes non-trivial. Therefore, a robust, reliable and computationally tractable modelling framework that can predict the density evolution during the sintering of any powder material becomes particularly valuable for successful process implementation, optimization and design of experiments.

6. Conclusions and outlook

The linear-viscous case of the SOVS model, based on the theories of irreversible deformation (flow) of porous bodies, was implemented in FEM code. A novel improved and simplified implicit integration scheme for the state variables was proposed to avoid the inverse of the Jacobian at each integration point using a staggered implicit solution scheme, resulting in a reduction factor of 50 (using the same solid element) to 1000 (using the solid-like shell element) in terms of computational cost. The modelling strategy was verified by comparing the simulated relative density evolutions to analytical solutions, as well as to sintering experiments. The utilization of solid-like shell elements with the SOVS constitutive model of sintering opened the possibility of predicting bending and distortion problems in bilayers induced by differential shrinkage, which are common in the manufacturing of components for energy and electronics applications, with a relatively small computational cost. As an example, the computation cost (CPU time) of the benchmark simulation of Garino's bilayer bar experiment [47] was reduced by approximately three orders of magnitude, enabling the simulation of hours-long sintering processes with a normal laptop/computer in short time frames.

Apart from Garino's bilayer bar experiment, Garino's bilayer disc experiment, which is close to real applications, was also simulated for a quantitative comparison. The agreement between simulated results and experiments is good, with the differences/errors up to 4% and 8% for the bilayer bar and disc experiments, respectively. To further improve the accuracy, a new sintering experiment was carried out using a ceramic material that is particularly relevant in bilayer and membrane processing for energy applications (catalysis for hydrogen generation): $LaWO_{54}$. A new method to determine the temperature and micro-structure influence on the material viscosity was proposed and validated with this independent sintering experiment. Unlike previous studies that focused mainly on the heating stage of sintering, our sintering experiment and simulation covered the full cycle: heating, holding and cooling stages. The simulation accurately predicted the final dimensions of sintered pellet with errors up to around 3%. Furthermore, the relative density evolution predicted by the simulations was also compared to experimental values that originate from different measurement methods, confirming the agreement and accuracy of the proposed model.

These SOVS model developments open pathways towards fast, accurate and versatile continuum scale simulations of a multitude of sintering processes. The differential shrinkage during co-sintering of bilayer or even trilayer parts with different materials or porosity levels in each layer can now be smoothly simulated in virtual frameworks. Further improvements in the model details, e.g. to incorporate micro-features such as grain growth, will be studied in more detail in future works.

Declaration of competing interest

The authors declare that they have no known competing financial interests or personal relationships that could have appeared to influence the work reported in this paper.

Acknowledgements

The financial support through the "AMAZING" project (grant no. TKITOEAmazing) from Dutch top consortia for Knowledge and Innovation programme Energy and Industry (TKI E&I) is gratefully acknowledged. The authors would like to thank Dr. Wendelin Deibert and Prof. Wilhelm Albert Meulenberg (Institute of Energy and Climate Research, Materials Synthesis and Processing, Forschungszentrum Jülich, Germany) for providing the materials for the experimental validation steps. The authors would also like to thank MSc. Michel Drazkowsky and Prof. Arian Nijmeijer (Inorganic Membranes, University of Twente, the Netherlands) for their support with pressing and sintering experiments. The Institute for Sustainable Process Technology (ISPT) is also acknowledged for the help in coordinating the project.

Appendix. Reduction and implementation of implicit solution scheme

From Eq. (16) we need to minimize the residual and iteratively solve 13 unknown state variables every timestep for the set of implicit equations proposed. This means at each timestep and at each integration point, Eq. (16) needs to be solved to reach local convergence. This it will quickly lead to high computational costs once 3D solid elements and/or longer total simulation times are employed, which is typically the case for a traditional free sintering process. Therefore, a reduction of the implicit equations is applied such that only 1 unknown state variable needs to be solved at every timestep at the integration points.

A.1. Implicit equation associated with elastic strain

The residual of the elastic strain results from the strain decomposition Eq. (1),

$$\boldsymbol{f}_{\varepsilon_e} = \Delta\boldsymbol{\varepsilon}_e + \Delta\boldsymbol{\varepsilon}_i - \Delta\boldsymbol{\varepsilon} \tag{1A}$$

A.2. Implicit equation associated with inelastic strain

The residual of the inelastic strain is then formed from the general implicit solution routine Eq. (15)

$$\boldsymbol{f}_{\varepsilon_i} = \Delta\boldsymbol{\varepsilon}_i - \Delta t\dot{\boldsymbol{\varepsilon}}_i^{t+\Delta t} = \Delta\boldsymbol{\varepsilon}_i - \Delta t\frac{\boldsymbol{\sigma}'}{2\eta\phi} - \Delta t\frac{\mathrm{tr}(\boldsymbol{\sigma}) - 3P_L}{18\eta\psi}\boldsymbol{I} \tag{2A}$$

Note that all the time dependent variables $(\boldsymbol{\sigma}, P_L, \eta, \psi)$ refer to the unknown values at the next time step, i.e. $t + \Delta t$.

A.3. Evolution of relative density

From Eq. (9), the change of density can be derived within one timestep, leading to its residual form:

$$f_\rho = \Delta\rho + \rho^{t+\Delta t}\Delta e \tag{3A}$$

where Δe is the trace of the change of inelastic strain tensor $\mathrm{tr}(\Delta\boldsymbol{\varepsilon}_i)$.

As $\Delta\rho$ can be expressed as a function of $\Delta\boldsymbol{\varepsilon}_i$, we could explicitly calculate the density evolution and eliminate this unknown from the solution routine. Integrating Eq. (9) over Δt:

$$\rho^{t+\Delta t} = \rho^t \exp(\Delta e) \tag{4A}$$

A.4. Elimination of the inelastic strain

Combining Eqs. (1A), (2A) and (3A), it is more efficient to remove part of the unknowns and keep only two variables for solving: $\Delta\boldsymbol{\varepsilon}_e$ and $\mathrm{tr}(\Delta\boldsymbol{\varepsilon}_i)$. Then from Eqs. (1A) and (2A), we obtain a new system of equations:

$$\begin{cases} \boldsymbol{f}_{\varepsilon_e} = \Delta\boldsymbol{\varepsilon}_e + \Delta t\frac{\boldsymbol{\sigma}'}{2\eta\phi} + \frac{1}{3}\Delta e\boldsymbol{I} - \Delta\boldsymbol{\varepsilon} \\ f_e = \Delta e - 3\Delta t\frac{\mathrm{tr}(\boldsymbol{\sigma}) - 3P_L}{18\eta\psi} \end{cases} \tag{5A}$$

For brevity, we hide the parameter dependencies in the above set of equations. All the parameters are evaluated based on the dependent state variable's values at the next timestep, e.g., $\boldsymbol{\sigma}(\rho^{t+\Delta t})$, $P_L(\rho^{t+\Delta t})$, $\eta(T^{t+\Delta t}, \rho^{t+\Delta t})$, $\psi(\rho^{t+\Delta t})$, while the relative density $\rho(\Delta e)$ is given by Eq. (4A).

In order to obtain simple and clear derivatives, Eq. (5A) can be rewritten as,

$$\begin{cases} \boldsymbol{f}_{\varepsilon_e} = \Delta\boldsymbol{\varepsilon}_e + \Delta t A\boldsymbol{\sigma}' + \frac{1}{3}\Delta e\boldsymbol{I} - \Delta\boldsymbol{\varepsilon} \\ f_e = \Delta e - 3\Delta t[B\,\mathrm{tr}(\boldsymbol{\sigma}) - C] \end{cases} \tag{6A}$$

where

$$\begin{cases} A(\rho^{t+\Delta t}(\Delta e)) = \frac{1}{2\eta\phi} \\ B(\rho^{t+\Delta t}(\Delta e)) = \frac{1}{18\eta\psi} \\ C(\rho^{t+\Delta t}(\Delta e)) = 3B(\rho^{t+\Delta t}(\Delta e)) \cdot P_L \end{cases}$$

A.5. Solving scheme of reduced system of implicit equations

In Eq. (6A), we have 7 unknowns with Δe and $\Delta \varepsilon_e$ that consists of 6 independent strain components. To solve them using the Newton–Raphson method, one needs to construct a 7 × 7 Jacobian:

$$\boldsymbol{J} = \begin{bmatrix} \frac{\partial f_{\varepsilon_e}}{\partial \Delta \varepsilon_e} & \frac{\partial f_{\varepsilon_e}}{\partial \Delta e} \\ \frac{\partial f_e}{\partial \Delta \varepsilon_e} & \frac{\partial f_e}{\partial \Delta e} \end{bmatrix}$$

where

$$\frac{\partial \boldsymbol{f}_{\varepsilon_e}}{\partial \Delta \boldsymbol{\varepsilon}_e} = {}^4\boldsymbol{I} + 2\Delta t \mu A({}^4\boldsymbol{I} - \frac{1}{3}\boldsymbol{I} \otimes \boldsymbol{I})$$

$$\frac{\partial \boldsymbol{f}_{\varepsilon_e}}{\partial \Delta e} = \frac{1}{3}\boldsymbol{I} + \Delta t \frac{\partial A}{\partial \rho}\frac{\partial \rho}{\partial \Delta e}\boldsymbol{\sigma}'$$

$$\frac{\partial f_e}{\partial \Delta \boldsymbol{\varepsilon}_e} = -3\Delta t B(2\mu + 3\lambda)\boldsymbol{I}$$

$$\frac{\partial f_e}{\partial \Delta e} = 1 - 3\Delta t \left[\frac{\partial B}{\partial \rho}\frac{\partial \rho}{\partial \Delta e}\mathrm{tr}(\boldsymbol{\sigma}) - \frac{\partial C}{\partial \rho}\frac{\partial \rho}{\partial \Delta e}\right]$$

For all the terms inside Jacobian:

$$\frac{\partial \rho^{t+\Delta t}}{\partial \Delta e} = -\rho^t \exp(-\Delta e) = -\rho^{t+\Delta t}$$

$$\frac{\partial \phi}{\partial \rho^{t+\Delta t}} = 2\rho^{t+\Delta t}$$

$$\frac{\partial \psi}{\partial \rho^{t+\Delta t}} = -\frac{2}{3}\frac{\rho^2(2\rho - 3)}{(\rho - 1)^2}$$

$$\frac{\partial A}{\partial \phi} = -\frac{1}{2\eta\psi^2}$$

$$\frac{\partial B}{\partial \psi} = -\frac{1}{18\eta\phi^2}$$

$$\frac{\partial A}{\partial \Delta e} = \frac{\partial A}{\partial \phi}\frac{\partial \phi}{\partial \rho}\frac{\partial \rho}{\partial \Delta e}$$

$$\frac{\partial B}{\partial \Delta e} = \frac{\partial B}{\partial \psi}\frac{\partial \psi}{\partial \rho}\frac{\partial \rho}{\partial \Delta e}$$

$$\frac{\partial P_L}{\partial \rho} = \frac{6\alpha}{r_p}\rho$$

$$\frac{\partial P_L}{\partial \Delta e} = \frac{\partial P_L}{\partial \rho}\frac{\partial \rho}{\partial \Delta e}$$

$$\frac{\partial C}{\partial \Delta e} = 3P_L\frac{\partial B}{\partial \Delta e} + 3B\frac{\partial P_L}{\partial \Delta e}$$

A.6. Elimination of the elastic strain

As the deviatoric part of $\boldsymbol{\varepsilon}_i$ is linear with the stress deviator, Eq. (6A) can be further reduced to only a single scalar unknown Δe.

Using Eq. (2):

$$\mathrm{tr}(\Delta \boldsymbol{\sigma}) = (3\lambda + 2\mu)\mathrm{tr}(\Delta \varepsilon - \Delta \varepsilon_i) \tag{7A}$$

Putting into Eq. (6A), we obtain:

$$\begin{aligned} f_e &= \Delta e - 3\Delta t\left[B\mathrm{tr}(\boldsymbol{\sigma}^{t+\Delta t}) - C\right] \\ &= \Delta e - 3\Delta t\left[B\mathrm{tr}(\boldsymbol{\sigma}^t) + B\mathrm{tr}(\Delta\boldsymbol{\sigma}) - C\right] \\ &= \Delta e - 3\Delta t\left[B\mathrm{tr}(\boldsymbol{\sigma}^t) + B(3\lambda + 2\mu)\mathrm{tr}(\Delta\varepsilon - \Delta\varepsilon_i) - C\right] \end{aligned} \tag{8A}$$

Then the tangent can be derived as:

$$\begin{aligned} \frac{\partial f_e}{\partial \Delta e} = 1 - 3\Delta t \bigg[& \frac{\partial B}{\partial \Delta e}\mathrm{tr}(\boldsymbol{\sigma}^t) + (3\lambda + 2\mu)\mathrm{tr}(\Delta\varepsilon)\frac{\partial B}{\partial \Delta e} \\ & -(3\lambda + 2\mu)(B + \frac{\partial B}{\partial \Delta e}\Delta e) - \frac{\partial C}{\partial \Delta e}\bigg] \end{aligned} \tag{9A}$$

References

[1] R. German, Sintering: From Empirical Observations to Scientific Principles, Butterworth-Heinemann, 2014.

[2] A. Zavaliangos, J. Missiaen, D. Bouvard, Anisotropy in shrinkage during sintering, Sci. Sinter. 38 (1) (2006) 13–25, http://dx.doi.org/10.2298/SOS0601013Z.

[3] J.-M. Missiaen, Solid-state spreading and sintering of multiphase materials, Mater. Sci. Eng. A 475 (1–2) (2008) 2–11, http://dx.doi.org/10.1016/j.msea.2007.01.160.

[4] C. Djangang, A. Elimbi, U. Melo, G. Lecomte, C. Nkoumbou, J. Soro, J.-P. Bonnet, P. Blanchart, D. Njopwouo, Sintering of clay-chamotte ceramic composites for refractory bricks, Ceram. Int. 34 (5) (2008) 1207–1213, http://dx.doi.org/10.1016/j.ceramint.2007.02.012.

[5] W. Deibert, M.E. Ivanova, W.A. Meulenberg, R. Vaßen, O. Guillon, Preparation and sintering behaviour of La5.4WO12-δ asymmetric membranes with optimised microstructure for hydrogen separation, J. Membr. Sci. 492 (2015) 439–451, http://dx.doi.org/10.1016/j.memsci.2015.05.065.

[6] W. Deibert, F. Schulze-Küppers, E. Forster, M.E. Ivanova, M. Müller, W.A. Meulenberg, Stability and sintering of MgO as a substrate material for Lanthanum Tungstate membranes, J. Eur. Ceram. Soc. 37 (2) (2017) 671–677, http://dx.doi.org/10.1016/j.jeurceramsoc.2016.09.033.

[7] K. Leonard, W. Deibert, M.E. Ivanova, W.A. Meulenberg, T. Ishihara, H. Matsumoto, Processing ceramic proton conductor membranes for use in steam electrolysis, Membranes 10 (11) (2020) 339, http://dx.doi.org/10.3390/membranes10110339.

[8] M. Jurisch, T. Studnitzky, O. Andersen, B. Kieback, 3D screen printing for the fabrication of small intricate Ti-6Al-4V parts, Powder Metall. 58 (5) (2015) 339–343, http://dx.doi.org/10.1179/0032589915Z.000000000255.

[9] S.L. Sing, W.Y. Yeong, F.E. Wiria, B.Y. Tay, Z. Zhao, L. Zhao, Z. Tian, S. Yang, Direct selective laser sintering and melting of ceramics: A review, Rapid Prototyp. J. 23 (3) (2017) 611–623, http://dx.doi.org/10.1179/0032589915Z.000000000255.

[10] E. Torresani, D. Giuntini, C. Zhu, T. Harrington, K.S. Vecchio, A. Molinari, R.K. Bordia, E.A. Olevsky, Anisotropy of mass transfer during sintering of powder materials with pore–particle structure orientation, Metall. Mater. Trans. A 50 (2) (2019) 1033–1049, http://dx.doi.org/10.1007/s11661-018-5037-x.

[11] E. Torresani, R. German, R. Huff, E. Olevsky, Influence of gravity on sintering of 3D-printed powder components, J. Am. Ceram. Soc. 105 (1) (2022) 131–146, http://dx.doi.org/10.1111/jace.18056.

[12] G. Largiller, L. Dong, D. Bouvard, C.P. Carry, A. Gabriel, Constitutive modeling of the behaviour of cermet compacts during reaction sintering, Powder Technol. 208 (2) (2011) 496–502, http://dx.doi.org/10.1016/j.powtec.2010.08.049.

[13] G. Largiller, D. Bouvard, C.P. Carry, A. Gabriel, J. Müller, T. Staab, Deformation and cracking during sintering of bimaterial components processed from ceramic and metal powder mixes. Part I: Experimental investigation, Mech. Mater. 53 (2012) 123–131, http://dx.doi.org/10.1016/j.mechmat.2012.04.002.

[14] G. Largiller, L. Dong, D. Bouvard, C.P. Carry, A. Gabriel, Deformation and cracking during sintering of bimaterial components processed from ceramic and metal powder mixes. Part II: Numerical simulation, Mech. Mater. 53 (2012) 132–141, http://dx.doi.org/10.1016/j.mechmat.2012.05.012.

[15] T.T. Molla, R. Bjørk, E. Olevsky, N. Pryds, H.L. Frandsen, Multi-scale modeling of shape distortions during sintering of bi-layers, Comput. Mater. Sci. 88 (2014) 28–36, http://dx.doi.org/10.1016/j.commatsci.2014.02.041.

[16] J. Rojek, S. Nosewicz, M. Maździarz, P. Kowalczyk, K. Wawrzyk, D. Lumelskyj, Modeling of a sintering process at various scales, Procedia Eng. 177 (2017) 263–270, http://dx.doi.org/10.1016/j.proeng.2017.02.210.

[17] K.-i. Mori, K. Osakada, T. Hirano, Finite element simulation of nonuniform shrinkage during sintering of ceramic products, in: Hot Isostatic Pressing—Theory and Applications, Springer, 1992, pp. 29–34, http://dx.doi.org/10.1007/978-94-011-2900-8_5.

[18] H. Zipse, Finite-element simulation of the die pressing and sintering of a ceramic component, J. Eur. Ceram. Soc. 17 (14) (1997) 1707–1713, http://dx.doi.org/10.1016/S0955-2219(97)00037-X.

[19] E.A. Olevsky, Theory of sintering: From discrete to continuum, Mater. Sci. Eng. R 23 (2) (1998) 41–100, http://dx.doi.org/10.1016/S0927-796X(98)00009-6.

[20] T. Kraft, H. Riedel, Numerical simulation of solid state sintering; Model and application, J. Eur. Ceram. Soc. 24 (2) (2004) 345–361, http://dx.doi.org/10.1016/S0955-2219(03)00222-X.

[21] T.T. Molla, H.L. Frandsen, R. Bjørk, D.W. Ni, E. Olevsky, N. Pryds, Modeling kinetics of distortion in porous bi-layered structures, J. Eur. Ceram. Soc. 33 (7) (2013) 1297–1305, http://dx.doi.org/10.1016/j.jeurceramsoc.2012.12.019.

[22] A. Al-Qudsi, M. Kammler, A. Bouguecha, C. Bonk, B.-A. Behrens, Comparison between different numerical models of densification during solid-state sintering of pure aluminium powder, Prod. Eng. 9 (1) (2015) 11–24, http://dx.doi.org/10.1007/s11740-014-0574-7.

[23] D. Giuntini, I.W. Chen, E.A. Olevsky, Sintering shape distortions controlled by interface roughness in powder composites, Scr. Mater. 124 (2016) 38–41, http://dx.doi.org/10.1016/j.scriptamat.2016.06.024.

[24] D. Giuntini, E.A. Olevsky, Sintering stress of nonlinear viscous materials, J. Am. Ceram. Soc. 99 (11) (2016) 3520–3524, http://dx.doi.org/10.1111/jace.14550.

[25] C.L. Martin, D. Bouvard, S. Shima, Study of particle rearrangement during powder compaction by the Discrete Element Method, J. Mech. Phys. Solids 51 (4) (2003) 667–693, http://dx.doi.org/10.1016/S0022-5096(02)00101-1.

[26] A. Wonisch, O. Guillon, T. Kraft, M. Moseler, H. Riedel, J. Rödel, Stress-induced anisotropy of sintering alumina: Discrete element modelling and experiments, Acta Mater. 55 (15) (2007) 5187–5199, http://dx.doi.org/10.1016/j.actamat.2007.05.038.

[27] C.L. Martin, H. Camacho-Montes, L. Olmos, D. Bouvard, R.K. Bordia, Evolution of defects during sintering: Discrete element simulations, J. Am. Ceram. Soc. 92 (7) (2009) 1435–1441, http://dx.doi.org/10.1111/j.1551-2916.2009.03014.x.

[28] T. Rasp, C. Jamin, A. Wonisch, T. Kraft, O. Guillon, Shape distortion and delamination during constrained sintering of ceramic stripes: Discrete element simulations and experiments, J. Am. Ceram. Soc. 95 (2) (2012) 586–592, http://dx.doi.org/10.1111/j.1551-2916.2011.04939.x.

[29] S. Nosewicz, J. Rojek, K. Pietrzak, M. Chmielewski, Viscoelastic discrete element model of powder sintering, Powder Technol. 246 (2013) 157–168, http://dx.doi.org/10.1016/j.powtec.2013.05.020.

[30] S. Nosewicz, J. Rojek, M. Chmielewski, K. Pietrzak, Discrete element modeling of intermetallic matrix composite manufacturing by powder metallurgy, Materials 12 (2) (2019) 281, http://dx.doi.org/10.3390/ma12020281.

[31] B. Hugonnet, J.M. Missiaen, C.L. Martin, C. Rado, Effect of contact alignment on shrinkage anisotropy during sintering: Stereological model, discrete element model and experiments on NdFeB compacts., Mater. Des. 191 (2020) 108575, http://dx.doi.org/10.1016/j.matdes.2020.108575.

[32] Y.U. Wang, Computer modeling and simulation of solid-state sintering: A phase field approach, Acta Mater. 54 (4) (2006) 953–961, http://dx.doi.org/10.1016/j.actamat.2005.10.032.

[33] J. Deng, A phase field model of sintering with direction-dependent diffusion, Mater. Trans. 53 (2) (2012) 385–389, http://dx.doi.org/10.2320/matertrans.M2011317.

[34] S. Biswas, D. Schwen, J. Singh, V. Tomar, A study of the evolution of microstructure and consolidation kinetics during sintering using a phase field modeling based approach, Extreme Mech. Lett. 7 (2016) 78–89, http://dx.doi.org/10.1016/j.eml.2016.02.017.

[35] K. Chockalingam, V.G. Kouznetsova, O. van der Sluis, M.G.D. Geers, 2D Phase field modeling of sintering of silver nanoparticles, Comput. Methods Appl. Mech. Engrg. 312 (2016) 492–508, http://dx.doi.org/10.1016/j.cma.2016.07.002.

[36] S. Biswas, D. Schwen, V. Tomar, Implementation of a phase field model for simulating evolution of two powder particles representing microstructural changes during sintering, J. Mater. Sci. 53 (8) (2018) 5799–5825, http://dx.doi.org/10.1007/s10853-017-1846-3.

[37] J. Hötzer, M. Seiz, M. Kellner, W. Rheinheimer, B. Nestler, Phase-field simulation of solid state sintering, Acta Mater. 164 (2019) 184–195, http://dx.doi.org/10.1016/j.actamat.2018.10.021.

[38] R. Termuhlen, X. Chatzistavrou, J.D. Nicholas, H.-C. Yu, Three-dimensional phase field sintering simulations accounting for the rigid-body motion of individual grains, Comput. Mater. Sci. 186 (2021) 109963, http://dx.doi.org/10.1016/j.commatsci.2020.109963.

[39] E. Olevsky, V. Rikare, T.J. Garino, M.V. Braginsky, Simulation of Sintering of Layered Structures, Tech. Rep., Sandia National Lab.(SNL-NM), Albuquerque, NM (United States), 2000.

[40] V. Tikare, M. Braginsky, E.A. Olevsky, Numerical simulation of solid-state sintering: I, sintering of three particles, J. Am. Ceram. Soc. 86 (1) (2003) 49–53, http://dx.doi.org/10.1111/j.1151-2916.2003.tb03276.x.

[41] M. Braginsky, V. Tikare, E. Olevsky, Numerical simulation of solid state sintering, Int. J. Solids Struct. 42 (2) (2005) 621–636, http://dx.doi.org/10.1016/j.ijsolstr.2004.06.022.

[42] E.A. Olevsky, V. Tikare, T. Garino, Multi-scale study of sintering: A review, J. Am. Ceram. Soc. 89 (6) (2006) 1914–1922, http://dx.doi.org/10.1111/j.1551-2916.2006.01054.x.

[43] K. Wawrzyk, P. Kowalczyk, S. Nosewicz, J. Rojek, A constitutive model and numerical simulation of sintering processes at macroscopic level, AIP Conf. Proc. 1922 (1) (2018) 030011, http://dx.doi.org/10.1063/1.5019045.

[44] T.T. Molla, N. Pryds, R. Bjørk, Modeling Macroscopic Shape Distortions during Sintering of Multi-Layers, Technical University of Denmark, 2014.

[45] D. Giuntini, X. Wei, A.L. Maximenko, L. Wei, A.M. Ilyina, E.A. Olevsky, Initial stage of free pressureless spark-plasma sintering of vanadium carbide: Determination of surface diffusion parameters, Int. J. Refract. Met. Hard Mater. 41 (2013) 501–506, http://dx.doi.org/10.1016/j.ijrmhm.2013.06.009.

[46] M.W. Reiterer, K.G. Ewsuk, J.G. Argüello, An Arrhenius-type viscosity function to model sintering using the Skorohod Olevsky viscous sintering model within a finite element code, J. Am. Ceram. Soc. 89 (6) (2006) 1930–1935, http://dx.doi.org/10.1111/j.1551-2916.2006.01041.x.

[47] J.G. Argüello, M.W. Reiterer, K.G. Ewsuk, Verification, performance, validation, and modifications to the SOVS continuum constitutive model in a nonlinear large-deformation finite element code, J. Am. Ceram. Soc. 92 (7) (2009) 1442–1449, http://dx.doi.org/10.1111/j.1551-2916.2009.03008.x.

[48] D. Giuntini, E.A. Olevsky, C. Garcia-Cardona, A.L. Maximenko, M.S. Yurlova, C.D. Haines, D.G. Martin, D. Kapoor, Localized overheating phenomena and optimization of spark-plasma sintering tooling design, Materials (Basel, Switzerland) 6 (7) (2013) 2612–2632, http://dx.doi.org/10.3390/ma6072612.

[49] T.T. Molla, D.W. Ni, R. Bulatova, R. Bjørk, C. Bahl, N. Pryds, H.L. Frandsen, Finite element modeling of camber evolution during sintering of bilayer structures, J. Am. Ceram. Soc. 97 (9) (2014) 2965–2972, http://dx.doi.org/10.1111/jace.13025.

[50] B.T. Lester, Verification of the Skorohod-Olevsky Viscous Sintering (SOVS) Model, Tech. Rep., Sandia National Lab.(SNL-NM), Albuquerque, NM (United States), 2017, http://dx.doi.org/10.2172/1411315.

[51] K. Shinagawa, Micromechanical modelling of viscous sintering and a constitutive equation with sintering stress, Comput. Mater. Sci. 13 (4) (1999) 276–285, http://dx.doi.org/10.1016/S0927-0256(98)00132-3.

[52] V. Aquilanti, K.C. Mundim, M. Elango, S. Kleijn, T. Kasai, Temperature dependence of chemical and biophysical rate processes: Phenomenological approach to deviations from Arrhenius law, Chem. Phys. Lett. 498 (1) (2010) 209–213, http://dx.doi.org/10.1016/j.cplett.2010.08.035.

[53] M. Bischoff, E. Ramm, Shear deformable shell elements for large strains and rotations, Internat. J. Numer. Methods Engrg. 40 (23) (1997) 4427–4449, http://dx.doi.org/10.1002/(SICI)1097-0207(19971215)40:23%3C4427::AID-NME268%3E3.0.CO;2-9.

[54] H. Parisch, A continuum-based shell theory for non-linear applications, Internat. J. Numer. Methods Engrg. 38 (11) (1995) 1855–1883, http://dx.doi.org/10.1002/nme.1620381105.

[55] F. Hashagen, J. Schellekens, R. De Borst, H. Parisch, Finite element procedure for modelling fibre metal laminates, Compos. Struct. 32 (1–4) (1995) 255–264, http://dx.doi.org/10.1016/0263-8223(95)00083-6.

[56] J.J.C. Remmers, R. De Borst, G. Wells, Analysis of delamination growth with discontinuous solid-like shell elements, in: Proceedings of the Fifth World Congress on Computational Mechanics, WCCM V, Vienna University of Technology, Austria, 2002.

[57] J.J.C. Remmers, G.N. Wells, R. de Borst, A solid-like shell element allowing for arbitrary delaminations, Internat. J. Numer. Methods Engrg. 58 (13) (2003) 2013–2040, http://dx.doi.org/10.1002/nme.907.

[58] F. Hashagen, R. de Borst, Numerical assessment of delamination in fibre metal laminates, Comput. Methods Appl. Mech. Engrg. 185 (2–4) (2000) 141–159, http://dx.doi.org/10.1016/S0045-7825(99)00256-X.

[59] J. Arguello, V. Tikare, T. Garino, M. Braginsky, Three-Dimensional Simulation of Sintering Using a Continuum Modeling Approach, Sandia National Laboratories, 2003.

[60] A. Magrasó, R. Haugsrud, Effects of the La/W ratio and doping on the structure, defect structure, stability and functional properties of proton-conducting lanthanum tungstate La 28-x W 4+x O 54+δ . A review, J. Mater. Chem. A 2 (32) (2014) 12630–12641, http://dx.doi.org/10.1039/C4TA00546E.

[61] C. Manière, E. Saccardo, G. Lee, J. McKittrick, A. Molinari, E.A. Olevsky, Swelling negation during sintering of sterling silver: An experimental and theoretical approach, Results Phys. 11 (2018) 79–84, http://dx.doi.org/10.1016/j.rinp.2018.08.035.

[62] C. Manière, S. Chan, G. Lee, J. McKittrick, E.A. Olevsky, Sintering dilatometry based grain growth assessment, Results Phys. 10 (2018) 91–93, http://dx.doi.org/10.1016/j.rinp.2018.05.014.